Check for updates

A confinement of N-heterocyclic molecules in a metal–organic framework for enhancing significant proton conductivity†

My V. Nguyen, [ID] *[a] Thang B. Phan, [ID] [b] Man V. Tran,[c] Tuyet A. T. Nguyen[a] and Hung N. Nguyen[a]

A series of N-heterocyclic⊂VNU-23 materials have been prepared *via* the impregnation procedure of N-heterocyclic molecules into VNU-23. Their structural characterizations, PXRD, FT-IR, Raman, TGA, ^{1}H-NMR, SEM-EDX, and EA, confirmed that N-heterocyclic molecules presented within the pores of parent VNU-23, leading to a remarkable enhancement in proton conductivity. Accordingly, the composite with the highest loading of imidazole, $Im_{13.5}$⊂VNU-23, displays a maximum proton conductivity value of 1.58×10^{-2} S cm^{-1} (85% RH and 70 °C), which is ~4476-fold higher than H$^+$⊂VNU-23 under the same conditions. Remarkably, the proton conductivity of $Im_{13.5}$⊂VNU-23 exceeds the values at 85% RH for several of the reported high-performing MOF materials. Furthermore, $Im_{13.5}$⊂VNU-23 can retain a stable proton conductivity for more than 96 h, as evidenced by FT-IR and PXRD analyses. These results prove that this hybrid material possesses potential applications as a commercial proton exchange membrane fuel cell.

1. Introduction

Electrolyte materials have attracted much attention through transforming chemical energy into electric energy by chemical reactions. Currently, proton exchange membrane fuel cells (PEMFCs) are recognized as a new electrolyte material capable of clean and high-energy conversion.[1–4] Nafion, a perfluorosulfonic acid membrane, is extensively employed as a commercial PEMFC due to its high proton conductivity ($\sigma = 0.1$ S cm^{-1} at 98% relative humidity (RH) at 80 °C).[5] Nevertheless, the synthesis process for Nafion is complex, leading to limitations for scale-up.[6–8] Additionally, the high RH value (98%) requires a high cost to retain during long-term operation and drives flooding at the cathode, resulting in a performance loss of PEMs with only a minor temperature fluctuation.[1] To cope with these challenges, it is necessary to find novel alternative proton conductive materials by incorporating factors as (1) high proton conductive performance at low relative humidity (RH <98%), (2) extended operating time, (3) high chemical and thermal stability, and (4) effortless large-scale.[9–11]

Metal–organic frameworks (MOFs) are porous coordination materials generated from metal clusters and organic bridge linkers with many applications in adsorption and environmental treatment,[12–17] catalysis,[18–20] sensors,[21] and drug delivery.[22,23] Recently, MOFs have been proven to be promising candidates for proton transport with high proton conductivity.[24–26] Besides, the future PEMFCs are desired to act under high voltage and long-term conditions. To fulfill these lofty targets, there is a requirement for creating a new material class with high chemical and mechanical stability. Zirconium-based MOFs are an efficient response material because of contain robust metal–carboxylate bonds and rigid frameworks, thus opening the unique chances for using Zr-based MOFs as the expected proton conductive membrane. As reported, Zr–MOFs exhibited the proton conductivity reached the value of 10^{-3} to 10^{-2} S cm^{-1}.[27–30]

The fact revealed that the high-level proton movement relating to the enormous number of protons significantly enhanced the proton conductivity in MOFs. This is addressed through modifying the void space of the frameworks and organic linkers by functional groups (*e.g.*, –COOH, –OH, and –SO$_3$H)[29–33] or introducing guest molecules such as ammonia,[34,35] water,[36] and N-heterocyclic molecules (*e.g.*, triazole,[37] histamine,[30,38] and imidazole[29,39,40]). The imidazole derivatives are chosen as the efficient proton carrier agents due to their high polarity, which can favourably uptake water molecules from the external medium, leading to the optimal proton conduction pathway formation.[41–43] However, proton conductivity of imidazole derivatives@MOF composites is

[a] Faculty of Chemistry, Ho Chi Minh City University of Education, Ho Chi Minh City, 700000, Vietnam. E-mail: mynv@hcmue.edu.vn

[b] Center for Innovative Materials and Architectures (INOMAR), Vietnam National University-Ho Chi Minh (VNU-HCM), Ho Chi Minh City 721337, Vietnam

[c] University of Science, VNU-HCM, Ho Chi Minh City 721337, Vietnam

† Electronic supplementary information (ESI) available: Full characterization and proton conductivity measurement details. See DOI: 10.1039/d1ra08534d

reduced throughout extended behaviour intervals due to the release of N-heterocyclic molecules from the structure, even resulting in cathode contamination.[26,44] This is attributed to the lack of robust, appropriate interactions between N-heterocyclic molecules and the framework. Hence, it is urgent to seek substitute solutions for minimizing the loss of mentioned guest molecules from the MOF composites.

To retain durable and extended proton conductivity, in our previous work,[29] we suggested an anchoring strategy of imidazole molecules onto VNU-17, constructed from $Zr_6O_8(H_2O)_8(COO)_8$ cluster and 4-sulfonaphthalene-2,6-dicarboxylic acid linker, containing Brønsted acidic sites of sulfonic groups ($-SO_3H$). VNU-17 is like the harbors to trap the imidazole molecules *via* acid–base reaction of SO_3H groups and coordinated water molecules with imidazole molecules. As a result, the proton conductivity of $HIm_{11} \subset VNU$-17 reached 5.93×10^{-3} S cm^{-1} at 70 °C and 85% RH without any remarkable change of performance for at least 40 h. Inspired by this, we expect that if the amount of SO_3H is enhanced within Zr–MOFs, it will increase the anchoring possibility of imidazole derivative molecules into the structure through robust acid–base interactions, assisting an increase of the proton conductivity and prolongation of operating time in the composite membranes. This is a new approach to coping with the stated obstacles about releasing imidazole derivatives of the reported composites during the proton conduction. Additionally, the role of each N-heterocyclic molecule in the proton transfer process is also considered for selecting the most effective proton carrier agent.

Owing to this viable approach, we performed a research strategy, including (i) syntheses of Zr–MOF with high thermal and chemical strength by mixing Zr^{4+} salt and 4,8-disulfonaphthalene-2,6-dicarboxylic acid linker (H_4SNDC) containing two of SO_3H groups per a linker unit, termed VNU-23,[30] (ii) confinement of a series of N-heterocyclic molecules such as imidazole (Im), 2-methylimidazole (mIm), and benzimidazole (bIm) onto VNU-23 to obtain the hybrid materials as $Im_x \subset VNU$-23, $mIm_y \subset VNU$-23, and $bIm_z \subset VNU$-23, respectively, (iii) measurement of proton conductivity for these hybrid materials under low RH (<98%) and testing their performing intervals. As expected, $bIm_{3.7} \subset VNU$-23 and $mIm_{9.2} \subset VNU$-23 possess the maximum proton conductivity reached the value of 2.13×10^{-4} S cm^{-1} and 4.21×10^{-3} S cm^{-1} under 85% RH at 70 °C, respectively. Noteworthy, the proton conductivity of $Im_{13.5} \subset VNU$-23 is 1.58×10^{-2} S cm^{-1} (85% RH and 70 °C), which is ~1445-fold higher than that achieves for parent $H^+ \subset VNU$-23 ($\sigma = 1.10 \times 10^{-5}$ S cm^{-1} under 90% RH at 70 °C). Particularly, the high proton conductivity value of $Im_{13.5} \subset VNU$-23 can retain more than 96 h, which demonstrates the future applications of this composite material as commercial PEMFCs.

2. Experimental

2.1 Chemicals and general procedures

Zirconium oxychloride octahydrate ($ZrOCl_2 \cdot 8H_2O$, 98%), *N,N*-dimethylformamide (DMF, 99%), formic acid (HCOOH, 95%), imidazole (Im, 99%), 2-methylimidazole (mIm, 99%), benzimidazole (bIm, 99%), oleum (SO_3 in H_2SO_4, 50%), hydrochloric

acid (HCl, 37%), and anhydrous methanol (MeOH, 99%) were purchased from local vendors and employed without further purification. 4,8-Disulfonaphthalene-2,6-dicarboxylic acid (H_4SNDC) was prepared according to the previously reported synthetic method.[30]

Fourier transform infrared spectroscopy (FT-IR) measurements were carried out on a Jasco spectrometer with the Attenuated Total Reflectance (ATR) sampling method. Raman spectroscopy analysis was collected on a Horiba XploRA ONE 532 nm. Thermal gravimetric analyses (TGA) were measured on a LabSys Evo thermal analysis system under dry air flow and in the temperature range of 25–800 °C. Powder X-ray data were recorded on a Bruker D8 Advance using Ni filtered Cu Kα ($\lambda = 1.54718$ Å). Water adsorption and desorption curves were analyzed on a Belsorp-aqua3 instrument at ambient temperature. ^{1}H-NMR spectra were obtained on a Bruker Advance NEO-600 MHz spectrometer. Humidity was controlled by an Espec humidity chamber (SH-222). Scanning electron microscopy (SEM) image was performed on a Hitachi FESEM S-4800 microscope with accelerating voltage of 10 kV. Energy-dispersive X-ray (EDX) analysis was measured on a Horiba EDX H-7593 instrument. Elemental analyses of C, H, N, and S were performed using a LECO CHNS-932 analyzer. Low pressure N_2 adsorption analyses were analyzed on a Micromeritics 3Flex surface characterization analyzer.

The materials (120 mg) were ground and pelletized for the alternating current (ac) impedance spectroscopy analyses, which were conducted on a Gamry potentiostat Interface 1000 with the two-electrode method, and the frequencies ranged from 10^6 to 10 Hz with the applied voltage altered from 1 to 10 mV. The samples were pressed at 4.2 MPa with 13 mm diameter. The thickness of the pellets was analyzed by a Nikon SMZ1000 microscope, varying from 0.60 to 0.62 mm. The impedance spectra were collected under different RHs and temperatures, in which the stability of relative humidity was maintained using the saturated salt solutions placed inside the chamber. The pellets were balanced for at least 24 h at different temperatures and RH values to retain the persistent RH before measurements for all the ac impedance spectra. The proton conductivity was calculated using the equation $\sigma = L/SR$, where σ, L, S are the conductivity (S cm^{-1}), the thickness of the samples (cm), the surface area of the pellets (cm^2), respectively and R is the resistance of membrane (R_2) counted by fitting out the Nyquist plots using the equivalent circuit diagram (Fig. S8†) through Gamry Echem Analyst program.

2.2 Synthesis of $H^+ \subset VNU$-23

According to the previously reported work,[30] $H^+ \subset VNU$-23 was prepared by the solvothermal method. A mixture of H_4SNDC (0.825 g, 2.183 mmol), and $ZrOCl_2 \cdot 8H_2O$ (0.650 g, 2.025 mmol) was introduced into a 200 mL glass bottle including HCOOH and DMF (25 mL and 100 mL, respectively). The mixture was then sonicated for 10 min and heated at 120 °C for 48 h. Subsequently, the mixture was cooled to room temperature, yielding to the powder, namely pristine VNU-23. This product was washed by DMF (2 × 50 mL) for 72 h. The sample was

exchanged with a solution (10 × 10 mL), containing H_2SO_4 (0.3 M) with MeOH/H_2O solvent (v/v = 4/1) for 48 h. Next, the product was centrifuged, and washed by an excess amount of MeOH/H_2O (v/v = 4/1) to obtain a solution with pH = 5. Finally, the material was exchanged with MeOH (6 × 20 mL) for 48 h, dried, and activated under vacuum at 80 °C for 24 h to yield $H^+ \subset$ VNU-23.

2.3 Synthesis of $Im_{13.5} \subset$ VNU-23

The activated $H^+ \subset$ VNU-23 (100 mg) was soaked in 10 mL of MeOH solution of Im (5 M). The mixture was stirred at 40 °C for 48 h. Continuously, 10 mL of fresh MeOH solution of Im (5 M) was introduced the mixture to assure the saturated loading of Im onto $H^+ \subset$ VNU-23 and stirred for 24 h at 40 °C. Then, the sample was centrifuged, and washed with a copious amount of MeOH (3 × 2 mL) to remove Im molecules on the surface and within intercrystalline regions. The material was activated at room temperature under vacuum for 24 h to acquire $Im_{13.5} \subset$ VNU-23. FT-IR (cm^{-1}, ATR): 3130 (w), 1607 (m), 1571 (s), 1414 (s), 1360 (s), 1321 (m), 1184 (s), 1065 (m), 1035 (s), 927 (w), 812 (m), 763 (s), 658 (s), 612 (s). Anal. calcd (%) for $C_{88.5}H_{118.6}O_{68.3}N_{27}S_8Zr_6$ = $\{Zr_6O_8(H_2O)_8(C_{12}H_6O_{10}S_2)_4\}\cdot$ 13.5($C_3H_4N_2$)·12.3H_2O: C, 30.75; H, 3.43; N, 10.95; S, 7.41. Found: C, 31.19; H, 3.52; N, 11.21; S, 7.02.

2.4 Synthesis of $mIm_{9.2} \subset$ VNU-23

The activated $H^+ \subset$ VNU-23 (100 mg) was immersed in a MeOH solution of mIm (10 mL, 5 M). The mixture was stirred at 40 °C for 48 h. Subsequently, 10 mL of fresh MeOH solution of mIm (5 M) was introduced the mixture to obtain the saturated loading of mIm onto $H^+ \subset$ VNU-23 and stirred for 24 h at 40 °C. The solid was centrifuged and washed with an excess amount of MeOH (3 × 2 mL) to remove mIm molecules on the surface and within intercrystalline regions. The product was activated at room temperature under vacuum for 24 h to yield $mIm_{9.2} \subset$ VNU-23. FT-IR (cm^{-1}, ATR): 3146 (w), 1607 (m), 1567 (s), 1418 (s), 1363 (s), 1303 (w), 1180 (m), 1117 (m), 1034 (m), 920 (w), 812 (m), 766 (s), 657 (s), 614 (s). Anal. calcd (%) for $C_{84.8}H_{110.6}O_{63.7}N_{18.4}S_8Zr_6$ = $\{Zr_6O_8(H_2O)_8(C_{12}H_6O_{10}S_2)_4\}\cdot$ 9.2($C_4H_6N_2$)·7.7H_2O: C, 31.73; H, 3.45; N, 8.03; S, 7.98. Found: C, 31.95; H, 3.31; N, 7.62; S, 7.66.

2.5 Synthesis of $bIm_{3.7} \subset$ VNU-23

This composite was prepared with the same method as these materials above. The activated $H^+ \subset$ VNU-23 (100 mg) was immersed in a MeOH solution of bIm (10 mL, 5 M). The mixture was stirred at 40 °C for 48 h. Subsequently, 10 mL of fresh MeOH solution of bIm (5 M) was introduced the mixture to acquire the saturated loading of bIm onto $H^+ \subset$ VNU-23 and stirred for 24 h at 40 °C. Similarly, the material was centrifuged, and washed with an excess amount of MeOH (3 × 2 mL) to ensure the removal of bIm molecules on the surface and within intercrystalline regions. The solid was activated at room temperature under vacuum for 24 h to obtain $bIm_{3.7} \subset$ VNU-23. FT-IR (cm^{-1}, ATR): 3101 (w), 1607 (m), 1569 (s), 1417 (s), 1364 (s), 1298 (w), 1179 (m), 1119 (m), 1036 (s), 924 (w), 812 (m), 767 (s), 658 (s), 611 (s). Anal. calcd (%) for $C_{66.9}H_{87.4}O_{71.6}N_{5.4}S_8Zr_6$ =
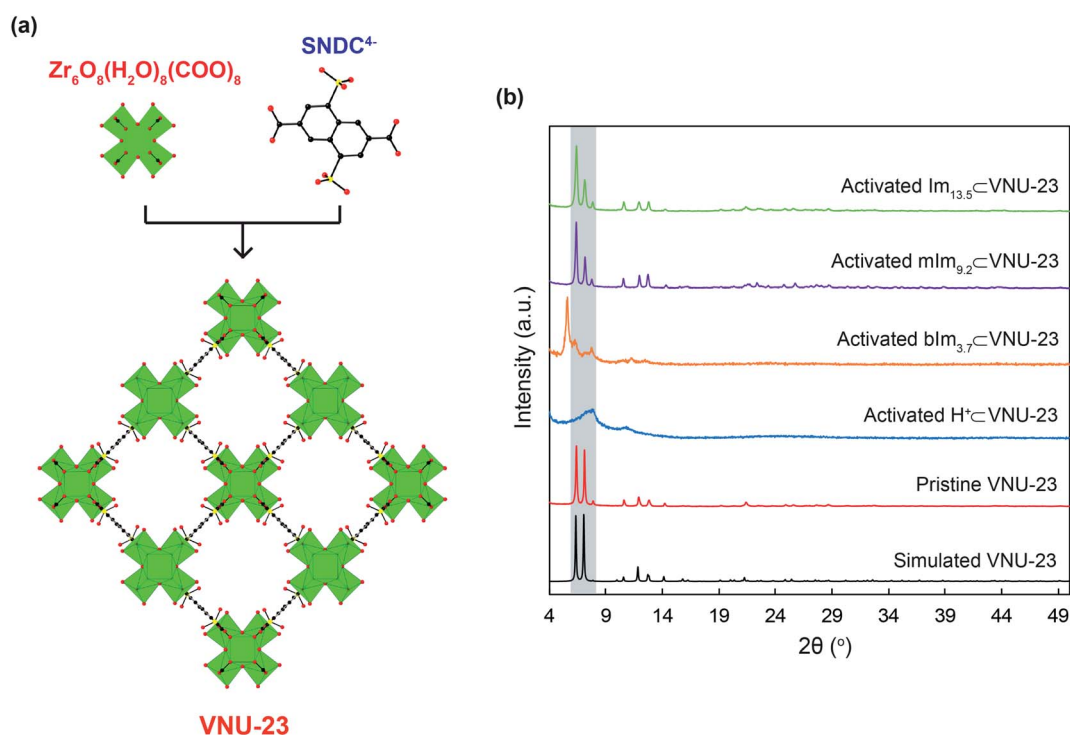

Fig. 1 (a) The structure of VNU-23 backbone is constructed from $Zr_6O_8(H_2O)_8(COO)_8$ and ditopic SNDC^{4-} linkers[30] and (b) PXRD pattern of simulated VNU-23 (black) in comparison with pristine VNU-23 (red), activated $H^+ \subset$ VNU-23 (blue), $bIm_{3.1} \subset$ VNU-23 (orange), $mIm_{9.2} \subset$ VNU-23 (purple), and $Im_{13.5} \subset$ VNU-23 (green). Atom colors: Zr, green polyhedra; C, black; O, red; S, yellow. All H atoms are omitted for clarity.

$\{Zr_6O_8(H_2O)_8(C_{12}H_6O_{10}S_2)_4\}\cdot3.7(C_7H_6N_2)\cdot15.6H_2O$: C, 29.25; H, 3.08; N, 3.42; S, 8.44. Found: C, 29.41; H, 2.95; N, 3.22; S, 8.17.

3. Results and discussion

3.1 Synthesis and characterization

Based on the previously published study,[30] VNU-23 was generated by blending $ZrOCl_2\cdot8H_2O$ salt and H_4SNDC linker in DMF solvent with formic acid as a modular for orienting the cluster structure and supporting the crystal nucleation. Subsequently, the mixture was heated at 120 °C for 48 h. In an attempt to understand the confinement mechanism of N-heterocyclic molecules onto VNU-23 for achieving the optimal proton transport pathway, there is a need to recall the structure of VNU-23. VNU-23 crystallizes in the space group of $I4/m$ and its unit cell parameter is $a = b = 17.7174$ Å and $c = 22.4865$ Å.[30] Four connected $SNDC^{4-}$ linkers and 8-connected $Zr_6O_8(H_2O)_8(COO)_8$ clusters construct the VNU-23 framework. This leads to the generation of a three-dimensional network framework with bcu topology (Fig. 1a). Herein, dimethylammonium ions is created during the synthetic process of VNU-23, which incorporate with

SO_3^- ions of linkers to obtain the rigid framework, assisting the conformity of the structure in comparison with the simulated VNU-23 (Fig. 1b). In order to recover the SO_3H groups, pristine VNU-23 was immersed in H_2SO_4 solution (0.3 M) and washed until the liquor reached pH = 5 to acquire $H^+\subset$VNU-23. The activated $H^+\subset$VNU-23 is lost the structural order due to the versatility of SO_3H after rehabilitation.[45,46] Notwithstanding, the crystallinity is recovered as soaked in water and MeOH (Fig. S1†). With this phenomenon, we assume that $H^+\subset$VNU-23 possesses the packed sulfonic groups (SO_3H), which can facilitate for doping process of the imidazole derivatives within the pore *via* acid–base reaction (Fig. 2), leading to the formation of the rigid backbone to maintain the structural order. Accordingly, N-heterocyclic$\subset$VNU-23 materials were synthesized by using the activated $H^+\subset$VNU-23 adsorbed the solutions of Im, mIm, and bIm at 40 °C. The PXRD analyses were assigned as the original confirmations for the successful doping of N-heterocyclic molecules in the pores of $H^+\subset$VNU-23. Fig. 1b reveals that the PXRD patterns of activated $Im_{13.5}\subset$VNU-23 and $mIm_{9.2}\subset$VNU-23 are in good agreement with simulated VNU-23. This demonstrates the effective encapsulation of Im and
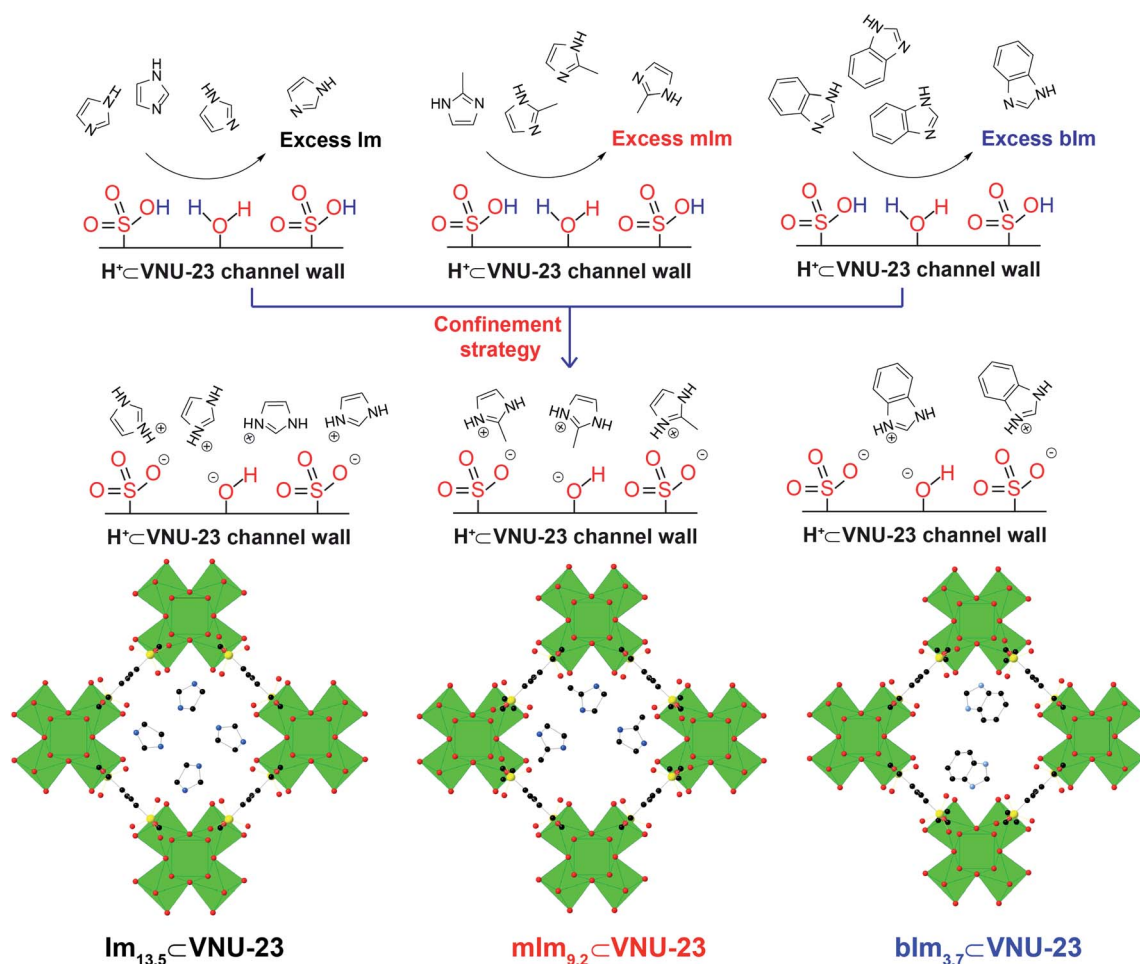

Fig. 2 Confinement strategy of N-heterocyclic molecules on the channel wall of $H^+\subset$VNU-23: plausible mechanism and the assumed position for encapsulating N-heterocyclic molecules on the channel wall of $H^+\subset$VNU-23. Atom colors: Zr, green polyhedra; C, black; O, red; S, yellow. All H atoms are omitted for clarity.
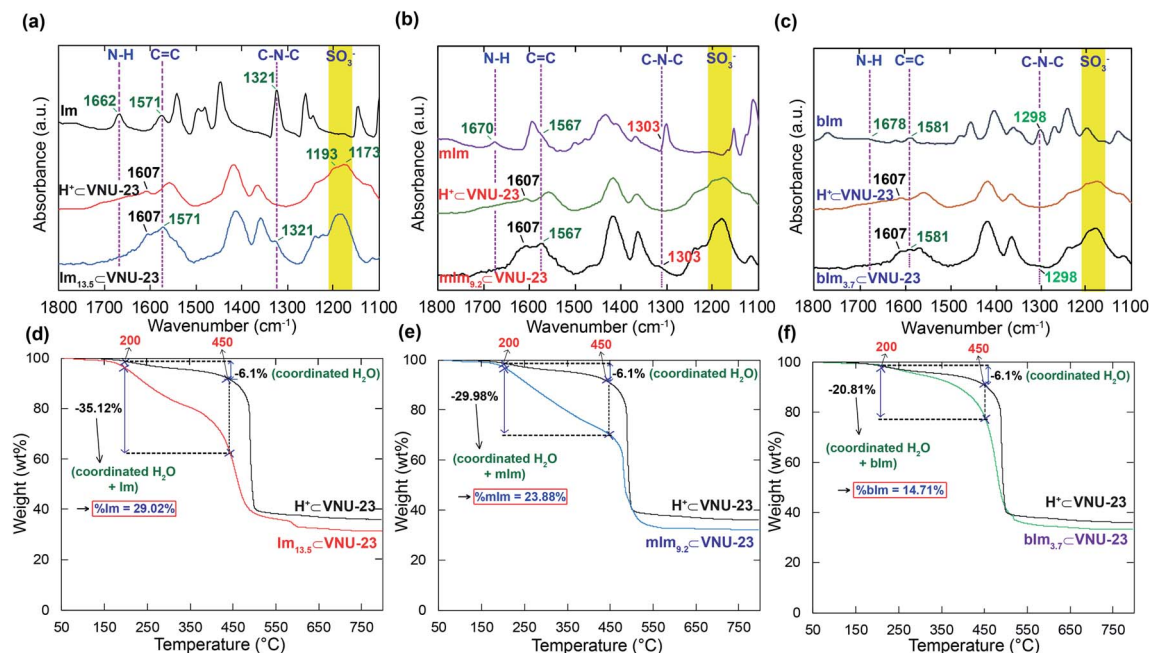
Fig. 3 Fourier transform-infrared spectroscopy analysis of N-heterocyclic⊂VNU-23: (a) $Im_{13.5}$⊂VNU-23, (b) $mIm_{9.2}$⊂VNU-23, (c) $bIm_{3.7}$⊂★ VNU-23 in comparison with H^+⊂VNU-23; thermal gravimetric analysis of N-heterocyclic⊂VNU-23 materials as compared to H^+⊂VNU-23 (d–f).

mIm onto H^+⊂VNU-23. In contrast, there is a deviation in the PXRD pattern of $bIm_{3.7}$⊂VNU-23 in comparison with the simulated VNU-23 (Fig. 1b). It can be explained that the molecular size of bIm is quite bulky, driving to its poor loading into the pores. Noteworthy, the content-dependent and time-dependent amounts of adsorbed Im, mIm, and bIm were also observed.

The maximum anchoring amounts of N-heterocyclic molecules were obtained at the adsorbing concentration of 5 M and time of 72 h (Fig. S4 and S5†). The quantities of Im, mIm, and bIm molecules anchored into the pores of H^+⊂VNU-23 were estimated by elemental analysis (EA). Subsequently, the Fourier transform infrared (FT-IR) spectra of $Im_{13.5}$⊂VNU-23, $mIm_{9.2}$⊂VNU-23, and $bIm_{3.7}$⊂VNU-23 are exhibited in Fig. 3a–c, distinguished with the IR spectrum of H^+⊂VNU-23 and the corresponding Im derivatives with the new signals located at 1298–1321 cm^{-1} and 1567–1581 cm^{-1}, which appear in the Im, mIm, and bIm spectra, but absent in H^+⊂VNU-23 range. These bands derive from C–N–C and C=C vibrations of Im, mIm, and bIm molecules, respectively. Besides, the absence of the adsorption signals at 1662, 1670, and 1678 cm^{-1} (confirmed to the N–H bending) in $Im_{13.5}$⊂VNU-23, $mIm_{9.2}$⊂VNU-23, and $bIm_{3.7}$⊂VNU-23 materials assign that all N-heterocyclic molecules are totally located within the pores of H^+⊂VNU-23. This is also evidenced by Raman spectroscopy analysis (Fig. S3†). Hence, the washing process of these composites by MeOH has entirely removed the abundant N-heterocyclic molecules from the surface and the intercrystalline regions. Furthermore, N-heterocyclic⊂VNU-23 materials exhibit the unique performance of weight loss from H^+⊂VNU-23. As given in Fig. 3d–f, H^+⊂VNU-23 shows a slope of weight loss (25–200 °C), and ~2 wt% is attributed to the release of

adsorbed water molecules on the surface, followed by a drop from 200 to 450 °C until the framework decomposition. The weight loss (200–450 °C) is ~6.1% and accounted for the loss of coordinated water from the clusters of $[Zr_6O_8(H_2O)_8(C_{12}H_6O_{10}-S_2)_4]$. However, N-heterocyclic⊂VNU-23 composites display a steeper drop (200–450 °C) assigned to releasing N-heterocyclic and coordinated water molecules. This situation is further confirmed by variable-temperature PXRD analyses (Fig. S2†), which reveal that the frameworks of $Im_{13.5}$⊂VNU-23 are thermally stable ≤450 °C.[29,30] Accordingly, the weight percentages of N-heterocyclic molecules in the range of 200–450 °C (29.02, 23.88, and 14.71% for $Im_{13.5}$⊂VNU-23, $mIm_{9.2}$⊂VNU-23, and $bIm_{3.7}$⊂VNU-23, respectively) are determined that there are ~13.9 Im, 8.9 mIm, and 3.4 bIm molecules per formula unit of $[Zr_6O_8(H_2O)_8(C_{12}H_6O_{10}S_2)_4]$ loaded in the framework of H^+⊂VNU-23.[29,30,39] Particularly, $Im_{13.5}$⊂VNU-23 sample was digested in acidic condition to perform ^{1}H-NMR measurements. From the resulting data, an imidazolium/H_4SNDC ratio of 3.41 is determined (Fig. S5†). This corresponded to 13.6 Im molecules per a formula unit of VNU-23. These values are in good agreement with EA result in the experimental section. All of the stated evidence, achieved from EA, PXRD, FT-IR, Raman, TGA, and ^{1}H-NMR measurements perceive that the N-heterocyclic molecules have been successfully immobilized into the framework of VNU-23.

3.2 Proton conduction of N-heterocyclic⊂VNU-23

Water adsorption/desorption curve is considered the vital factor for proton transfer, which helps us choose a perfect cut-off point for optimal proton conduction pathway to minimize the effect of condensed water on the surface of the compressed

pellets, resulting in the reduction of condensed water in accurate measurements. Hence, previous to measuring the proton conductivity of the composites, the water adsorption/desorption experiments were conducted at 25 °C. As shown in Fig. 4a–e, the water is condensed at $P/P_o = 0.93$ for pristine VNU-23 and $H^+ \subset$ VNU-23 materials, observed by the steep increase of water uptake. Therefore, their cut-off point is selected at $P/P_o = 0.9$ (RH = 90%) for measuring their proton conductivity. Meanwhile, all N-heterocyclic⊂VNU-23 composites possess the adsorption curves with the water condensed at $P/P_o = 0.87$, thus the proton conductivities of these composites are performed as high as possible at $P/P_o = 0.85$ (RH = 85%). Particularly, it is noted that the uptake capacity of $Im_{13.5} \subset$ VNU-23 is slightly higher than $mIm_{9.2} \subset$ VNU-23 and $bIm_{3.7} \subset$ VNU-23 at 85% RH, despite the truth that the pores of $mIm_{9.2} \subset$ VNU-23 and $bIm_{3.7} \subset$ VNU-23 possess a greater loading space of water than that of $Im_{13.5} \subset$ VNU-23. This phenomenon is similar to the previous works,[29,30] and attributed to the total hydration of $Im_{13.5} \subset$ VNU-23 at the grain boundary until the water condensed on the surface of the compressed pellet at higher RH.

Through the structural characterizations of the N-heterocyclic⊂VNU-23 composites with the packed arrangement of sulfonate groups conjugated to the protonated N-heterocyclic molecules, ac impedance analyses were conducted on the pelletized samples to determine their proton conductivities.

The proton conductivity of these composites was measured at different RH values (50–85%) with an immobilized temperature of 70 °C and at various temperatures (30–70 °C) with a fixed RH of 85%. As illustrated in Section S6,† the Nyquist plots show a semicircle in the high-frequency range caused by bulk and grain boundary, together with a tail at the low-frequency region dealing with the mobile ions blocked by the electrode–electrode interface.[47] Here, the resistance of the materials was calculated from the Z'-axis intercept parameter.[38] Accordingly, the proton conductivity of $Im_{13.5} \subset$ VNU-23, $mIm_{9.2} \subset$ VNU-23, and $bIm_{3.7} \subset$ VNU-23 is significantly relative to the RH values, which increases together with rising RH value (Fig. 5). It can be ascribed to the variations in the mobile degree of water molecules in pore channels at different RHs. At higher RH, the water uptake capacity of the materials increases, which supports the transfer process of protons through hydrogen bonding networks, leading to the enhancement in conductivity. In addition, the vital role of confined N-heterocyclic molecules within the structure has been demonstrated via the maximum proton conductivity of 1.58×10^{-2} S cm^{-1} for $Im_{13.5} \subset$ VNU-23 correlated with 4.21×10^{-3} S cm^{-1} for $mIm_{9.2} \subset$ VNU-23, and 2.13×10^{-4} S cm^{-1} for $bIm_{3.7} \subset$ VNU-23 at the same condition (85% RH, 70 °C). It is interesting to note that the higher amount of encapsulated Im derivatives increases of proton conductivity in all RH values.
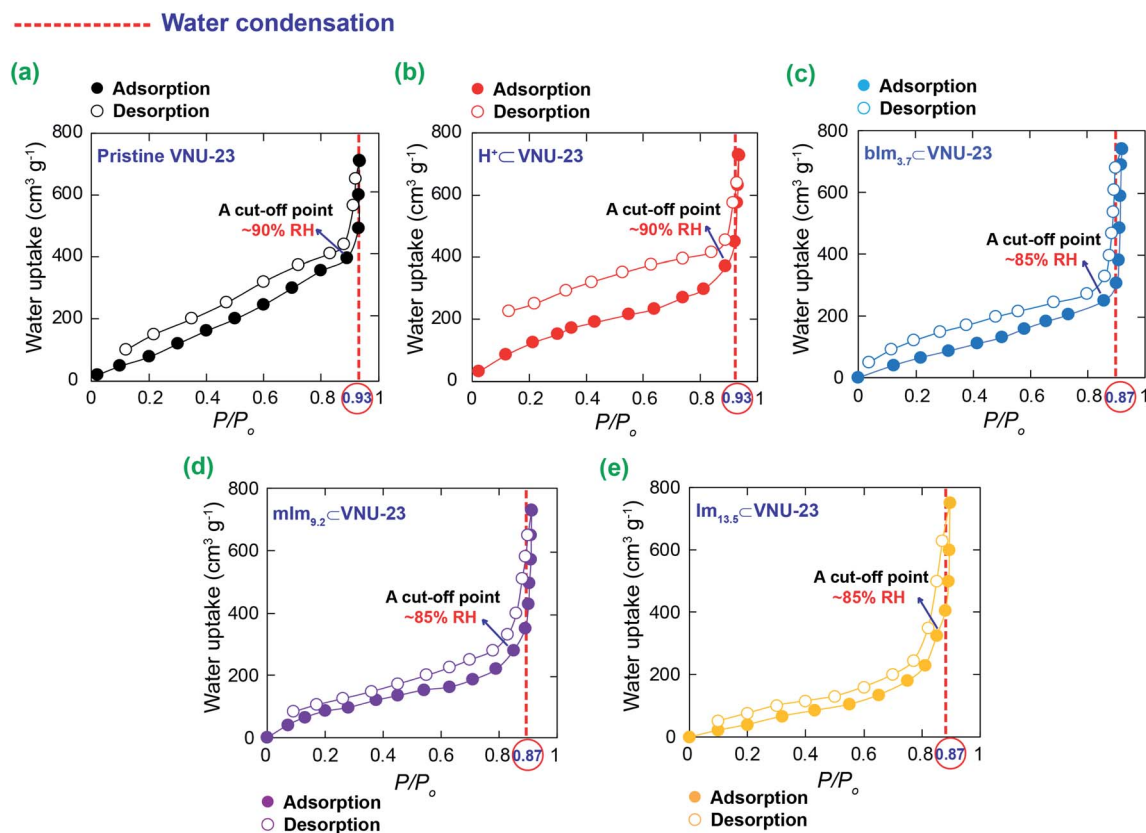

Fig. 4 The water uptake of N-heterocyclic⊂VNU-23 (c, d and e) in comparison with pristine VNU-23 (a) and $H^+ \subset$ VNU-23 (b) at 25 °C as a function of P/P_o.
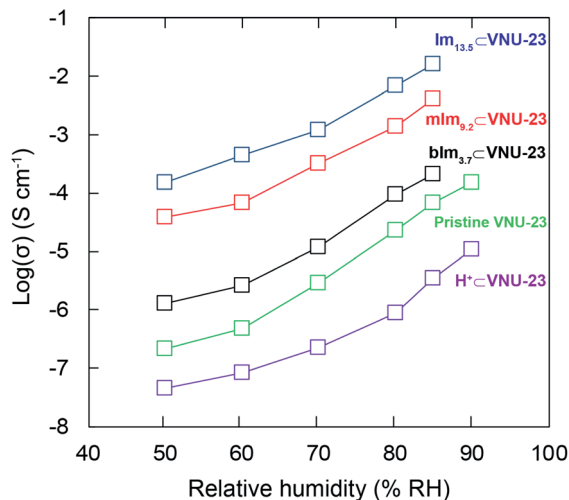

Fig. 5 Dependence of proton conductivity in $Im_{13.5} \subset VNU\text{-}23$ (blue), $mIm_{9.2} \subset VNU\text{-}23$ (red), and $bIm_{3.1} \subset VNU\text{-}23$ (black) in comparison with pristine VNU-23 (green) and $H^+ \subset VNU\text{-}23$ as a function of relative humidity at 70 °C.

Particularly, the proton conductivity of $Im_{13.5} \subset VNU\text{-}23$ is ~234 times higher than pristine VNU-23 with 8 dimethylammonium ions per a VNU-23 unit[30] (6.75×10^{-5} S cm^{-1} under 85% RH and 70 °C) and ~4476 times higher than $H^+ \subset VNU\text{-}23$ (3.53×10^{-6} S cm^{-1} under 85% RH and 70 °C). The fact shows that the sulfonic acid group, a strong acid, can devote H^+ ions to the conduction pathways more efficiently than dimethylammonium and imidazolium derivative ions, where H^+ is attached to the basic nitrogen sites of N-heterocyclic

Fig. 6 Time-dependent Nyquist plots of $Im_{13.5} \subset VNU\text{-}23$ (a); time-dependent proton conductivity of $Im_{13.5} \subset VNU\text{-}23$ conducted under 85% RH at 70 °C (b).

Table 1 The proton conductivity values for N-heterocyclic $\subset$ VNU-23 in comparison with high-performing proton conducting materials

Material	σ (S cm^{-1})	Conditions	Ref.
$Im_{13.5} \subset VNU\text{-}23$	1.58×10^{-2}	70 °C, 85% RH	This work
	5.82×10^{-3}	25 °C, 85% RH	
$mIm_{9.2} \subset VNU\text{-}23$	4.21×10^{-3}	70 °C, 85% RH	
$bIm_{3.7} \subset VNU\text{-}23$	2.13×10^{-4}	70 °C, 85% RH	
$Im/VNU\text{-}23$	3.04×10^{-6}	70 °C, 85% RH	
$Im@MOF\text{-}808$	3.45×10^{-2}	65 °C, 99% RH	39
	1.05×10^{-3}	25 °C, 85% RH	
$Im\text{-}Fe\text{-}MOF$	1.21×10^{-2}	60 °C, 98% RH	48
	5.56×10^{-6}	25 °C, 85% RH	
$HIm_{11} \subset VNU\text{-}17$	5.93×10^{-3}	70 °C, 85% RH	29
$PCMOF10$	7.50×10^{-3}	70 °C, 85% RH	50
$UiO\text{-}66\text{-}(CO_2H)_2$	1.25×10^{-4}	30 °C, 85% RH	45
$UiO\text{-}66$	3.16×10^{-8}	30 °C, 85% RH	
$HIm \subset UiO\text{-}67$	1.44×10^{-3}	120 °C	51

molecules, probably resulting in higher conductivity. However, the proton conductivity of pristine VNU-23 and N-heterocyclic $\subset$ VNU-23 samples is higher than parent $H^+ \subset VNU\text{-}23$, which is attributed to the full hydration of their grain boundary and pore channels addressed by the high polarity of imidazolium ions. This situation is also found in the reported studies.[29,30,39,48]

To further confirm the importance of Im molecules inside VNU-23 for enhancing the proton conductivity, we performed a series of additional experiments. In detail, $H^+ \subset VNU\text{-}23$ was mixed with pure Im at the same equivalent as the experimental section to obtain the new composite, termed Im/VNU-23. Section S7† reveals that Im/VNU-23 samples display a poor proton conductivity reached ~3.04×10^{-6} S cm^{-1} at 70 °C and 85% RH, which is ~5197 times lower than $Im_{13.5} \subset VNU\text{-}23$. This indicates that if Im molecules locate independently with the framework of VNU-23, they will not join and support favorably for the proton transport process of the material.

Moreover, it is seen that the proton conductivity of $Im_{13.5} \subset VNU\text{-}23$ at 70 °C and 85% RH betters the values at 85% RH for several reported MOF materials (Table 1). Even though $Im@MOF\text{-}808$ (ref. 39) exhibits the proton conductivity of 3.45×10^{-2} S cm^{-1} at 65 °C under.

99% RH, however, this RH value demands a high cost for retaining, and it quickly drives the flood at the cathode only by a minor temperature fluctuation, causing the decrease of proton conductivity. Additionally, investigating practical applications, the time-dependent conductivities of $Im_{13.5} \subset VNU\text{-}23$ have been performed under 85% RH at 70 °C. Fig. 6 shows that the proton conductivity of $Im_{13.5} \subset VNU\text{-}23$ is maintained for at least 96 h, without any remarkable reduction in performance. This indicates the desirable durability property of proton conductivity of $Im_{13.5} \subset VNU\text{-}23$ for prospective applications in PEMFCs. In order to inspect whether the structure of $Im_{13.5} \subset VNU\text{-}23$ changed after measuring long-term ac impedance analyses, FT-IR and PXRD analyses were performed to characterize its stability. As given in Section S8,† the FT-IR spectra and PXRD patterns of $Im_{13.5} \subset VNU\text{-}23$ are consistently
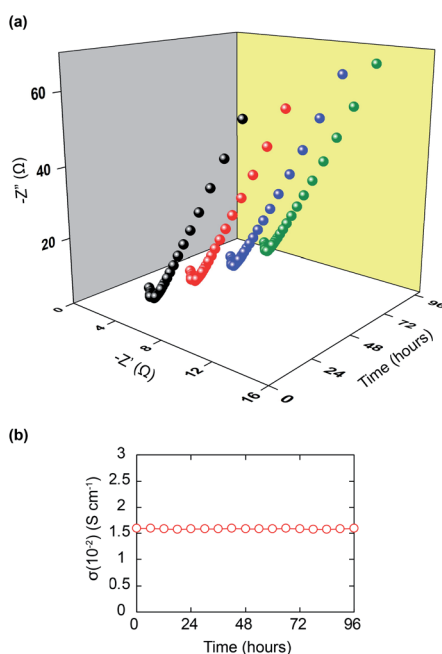
retained before and after ac impedance analyses (96 h), which demonstrate the high structural stability of this composite.

3.3 Plausible proton transport mechanism of N-heterocyclic⊂VNU-23

To understand the proton transfer proton mechanism in N-heterocyclic⊂VNU-23 materials, the proton conductivities of these composites with the temperature range from 30 to 70 °C under 85% RH are exhibited in Section S6.† It is realized that the proton conductivities of the materials show the trend of increasing with the increasing temperature. This can be explained by the higher temperatures providing energy for the dissociation process of the protons.[40] Besides, the activation energy (E_a) values under 85% RH of these composites were determined. The temperature dependence of proton conductivity could be calculated from eqn (1).[49]

$$\ln(\sigma T) = \ln(\sigma_o) - E_a/k_B T \qquad (1)$$

Where σ and σ_o are the proton conductivity and the pre-exponential factor, k_B and T are the Boltzmann constant and temperature. The activation energy is calculated from the slop of $1000 T^{-1}$ *vs.* $\ln(\sigma T)$.

In general, there are two mechanism types for the proton conduction in PEMFCs according to the activation energy, which reaches 0.1–0.4 eV for the Grotthuss mechanism and 0.4–0.9 eV for the vehicle mechanism.[26] Consequently, the Arrhenius plots of the hybrid materials are shown in Fig. 7. The E_a values of Im$_{13.5}$⊂VNU-23 and mIm$_{9.2}$⊂VNU-23 are 0.208 eV and 0.363 eV, which indicate the proton conduction occurred *via* a Grotthuss mechanism.

This can be ascribed that there are enormous hydrogen-bonding systems formed by external water molecules, coordinated water molecules, imidazolium, and 2-methylimidazolium ions, and sulfonate groups, which are the optimal proton transfer pathways for facilitating the jump of protons. Meanwhile, the Arrhenius fitting of bIm$_{3.7}$⊂VNU-23 results from the E_a of 0.427 eV demonstrates a vehicle mechanism. This may be because bIm molecules are loaded into the channel of VNU-23 with a small amount, resulting in the proton conduction through moving directionally into the channel.

4. Conclusion

In summary, the hybrid materials were successfully synthesized through a confinement approach of N-heterocyclic molecules into the pores of VNU-23 with suitable acid–base interactions. According to this structural characterization, N-heterocyclic⊂VNU-23 materials, Im$_{13.5}$⊂VNU-23, mIm$_{9.2}$⊂VNU-23, and bIm$_{3.7}$⊂VNU-23, exhibited high proton conductivity values under 85% RH and a moderately high temperature of 70 °C in comparison with parent H$^+$⊂VNU-23. Notably, Im$_{13.5}$⊂VNU-23 reveals the highest proton conductivity in all N-heterocyclic⊂VNU-23 composites and reaches a value of 1.58×10^{-2} S cm^{-1} (85% RH and 70 °C). To the best of our knowledge, the proton conductivity of Im$_{13.5}$⊂VNU-23 betters that of several of the highest performing MOF materials at ≤70 °C and 85% RH. In addition, Im$_{13.5}$⊂VNU-23 indicates the excellent durability and stability for proton conduction, which is retained without any reduction in performance of proton conductivity for at least 96 h. This finding is valuable for insight into the effect of N-heterocyclic molecules on the MOF structure for remarkably enhancing the proton conductivity, which is helpful for further synthetic procedures of new high proton conductivity composites.

Conflicts of interest

The authors maintain that they have no conflict of interest for this communication.

Acknowledgements

Notes and references

1 Q. Li, R. He, J. O. Jensen and N. Bjerrum, Approaches and recent development of polymer electrolyte membranes for fuel cells operating above 100 °C, *Chem. Mater.*, 2003, **15**, 4896–4915.

2 M. E. Scofield, H. Liu and S. S. Wong, A concise guide to sustainable PEMFCs: recent advances in improving both oxygen reduction catalysts and proton exchange membranes, *Chem. Soc. Rev.*, 2015, **44**, 5836–5860.

3 Y. Wang, K. S. Chen, J. Mishler, S. C. Cho and X. C. Adroher, A review of polymer electrolyte membrane fuel cells: technology, applications, and needs on fundamental research, *Appl. Energy*, 2011, **88**, 981–1007.
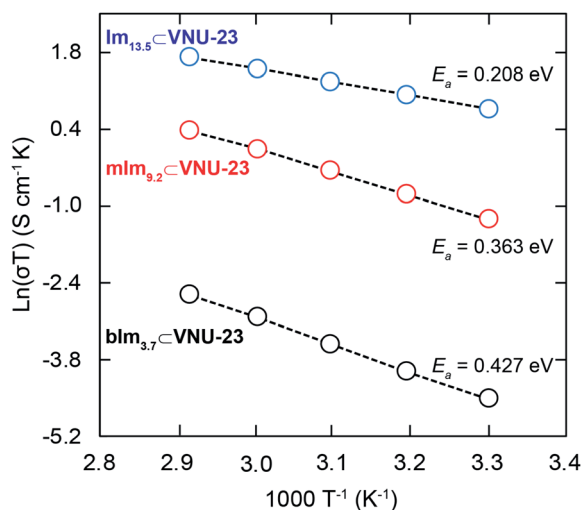
Fig. 7 Temperature-dependent proton conductivity measurements (30–70 °C) under 85% RH for Im$_{13.5}$⊂VNU-23 (blue), mIm$_{9.2}$⊂VNU-23 (red), and bIm$_{3.1}$⊂VNU-23 (black).

4 B. C. Steel and A. Heinzel, Materials for fuel-cell technologies, *Nature*, 2001, **414**, 345–352.

5 Z. Li, G. He, B. Zhang, Y. Cao, H. Wu, Z. Jiang and Z. Tiantian, En-hanced proton conductivity of Nafion hybrid membrane under differ-ent humidities by incorporating metal-organic frameworks with high phytic acid loading, *ACS Appl. Mater. Interfaces*, 2014, **6**, 9799–9807.

6 E. H. Majlan, D. Rohendi, W. R. W. Daud, T. Husaini and M. A. Haque, Electrode for proton exchange membrane fuel cells: A review, *Renewable Sustainable Energy Rev.*, 2018, **89**, 117–134.

7 G. He, J. Zhao, S. Hu, L. Li, Z. Li, Y. Li, Z. Li, H. Wu, X. Yang and Z. Jiang, Functionalized carbon nanotube via distillation precipitation polymerization and its application in Nafion-based composite membranes, *ACS Appl. Mater. Interfaces*, 2014, **6**, 15291–15301.

8 K. S. Lee, J. S. Spendelow, Y. K. Choe, C. Fujimoto and Y. S. Kim, An operationally flexible fuel cell based on quaternary ammonium-biphosphate ion pairs, *Nat. Energy*, 2016, **1**, 16120–16126.

9 Z. Guo, X. Xu, Y. Xiang, S. Lu and S. P. Jiang, New anhydrous proton exchange membranes for high-temperature fuel cells based on PVDF-PVP blended polymers, *J. Mater. Chem. A*, 2015, **3**, 148–155.

10 H. Wang, B. A. Holmberg, L. Huang, Z. Wang, A. Mitra, J. M. Norbeck and Y. Yan, Nafion-bifunctional silica composite proton con-ductive membranes, *J. Mater. Chem.*, 2002, **12**, 834–837.

11 S. J. Peighambardoust, S. Rowshanzamir and M. Amjadi, Review of the proton exchange membranes for fuel cell applications, *Int. J. Hydrogen Energy*, 2010, **35**, 9349–9384.

12 K. Adil, Y. Belmabkhout, R. S. Pillai, A. Cadiau, P. M. Bhatt, A. H. Assen, G. Maurin and M. Eddaoudi, Gas/vapour separation using ultra-microporous metal-organic frameworks: insights into the structure/separation relationship, *Chem. Soc. Rev.*, 2017, **46**, 3402–3430.

13 Y. Peng, V. Krungleviciute, I. Eryazici, J. T. Hupp, O. K. Farha and T. Yildirim, Methane storage in metal-organic frameworks: current records, surprise findings, and challenges, *J. Am. Chem. Soc.*, 2013, **135**, 11887–11894.

14 R. M. Rego, G. Sriram, K. V. Ajeya, H. Y. Jung, M. D. Kurkuri and M. Kigga, Cerium based UiO-66 MOF as a multipollutant adsorbent for universal water purification, *J. Hazard. Mater.*, 2021, **416**, 125941.

15 R. M. Rego, G. Kuriya, M. D. Kurkuri and M. Kigga, MOF based engineered materials in water remediation: Recent trends, *J. Hazard. Mater.*, 2021, **403**, 123605.

16 U. T. Uthappa, G. Sriram, O. R. Arvind, S. Kumar, H. Y. Jung, G. M. Neelgund, D. Losic and M. D. Kurkuri, Engineering MIL-100(Fe) on 3D porous natural diatoms as a versatile high performing platform for controlled isoniazid drug release, Fenton's catalysis for malachite green dye degradation and environmental adsorbents for Pb^{2+} removal and dyes, *Appl. Surf. Sci.*, 2021, **528**, 146974.

17 T. T. M. Bui, L. T. Nguyen, N. P. H. Pham, C. C. Tran, L. T. Nguyen, T. A. Nguyen, H. N. Nguyen and M. V. Nguyen, A new approach for ultra-high adsorption of cationic methylene blue in a Zr-sulfonic-based metal–organic framework, *RSC Adv.*, 2021, **11**, 36626–36635.

18 H. Liang, X. Jiao, C. Li and D. Chen, Flexible self-supported metal-organic framework mats with exceptionally high porosity for enhanced separation and catalysis, *J. Mater. Chem. A*, 2018, **6**, 334–341.

19 V. Stavila, R. Parthasarathi, R. W. Davis, F. El Gabaly, K. L. Sale, B. A. Simmons, S. Singh and M. D. Allendorf, MOF-based catalysts for selective hydrogenolysis of carbon-oxygen ether bonds, *ACS Catal.*, 2016, **6**, 55–59.

20 M. V. Nguyen, H. C. Dong, V. T. N. Truong, H. N. Nguyen, L. C. Luu, N. N. Dang and T. A. T. Nguyen, A new porphyrinic vanadium-based MOF constructed from infinite $V(OH)O_4$ chains: syntheses, characterization and photoabsorption properties, *New J. Chem.*, 2022, DOI: 10.1039/D1NJ05333G.

21 J. M. Li, R. Huo, X. Li and H. L. Sun, Lanthanide-organic frame-works constructed from 2,7-naphthalenedisulfonate and 1H-imidazo[4,5-f][1,10]-phenanthroline: synthesis, structure, and luminescence with near visible light excitation and magnetic properties, *Inorg. Chem.*, 2019, **58**, 9855–9865.

22 B. Lei, M. Wang, Z. Jiang, W. Qi, R. Su and Z. He, Constructing redox-responsive metal-organic framework nanocarriers for anti-cancer drug delivery, *ACS Appl. Mater. Interfaces*, 2018, **10**, 16698–16706.

23 S. Rojas, A. Arenas-Vivo and P. Horcajada, Metal-organic frameworks: a novel platform for combined advanced therapies, *Coord. Chem. Rev.*, 2019, **388**, 202–226.

24 X. Meng, H. N. Wang, S. Y. Song and H. J. Zhang, Proton-conducting crystalline porous materials, *Chem. Soc. Rev.*, 2017, **46**, 464–480.

25 M. V. Nguyen, H. C. Dong, D. M. Nguyen, N. H. Vu, T. T. Trinh and T. B. Phan, Effect of hydrogen-bonding networks in water on temperature and relative humidity dependence of proton conductivity in metal-organic frameworks, *J. Sci.: Adv. Mater. Devices*, 2021, **6**, 509–515.

26 P. Ramaswamy, N. E. Wong and G. K. H. Shimizu, MOFs as proton conductors-challenges and opportunities, *Chem. Soc. Rev.*, 2014, **43**, 5913–5932.

27 J. H. Cavka, S. Jakobsen, U. Olsbye, N. Guillou, C. Lamberti, S. Bordiga and K. P. Lillerud, A new zirconium inorganic building brick forming metal-organic frameworks with exceptional stability, *J. Am. Chem. Soc.*, 2018, **130**, 13850–13851.

28 H. L. Jiang, D. Feng, K. Wang, Z. Y. Gu, Z. Wei, Y. P. Chen and H. C. Zhou, An exceptionally stable, porphyrinic Zr metal-organic framework exhibiting pH-dependent fluorescence, *J. Am. Chem. Soc.*, 2013, **135**, 13934–13938.

29 T. H. N. Lo, M. V. Nguyen and T. N. Tu, An anchoring strategy leads to enhanced proton conductivity in a new metal-organic framework, *Inorg. Chem. Front.*, 2017, **4**, 1509–1516.

30 M. V. Nguyen, T. H. N. Lo, L. C. Luu, H. T. T. Nguyen and T. N. Tu, Enhancing proton conductivity in a metal-organic framework at T> 80 °C by an anchoring strategy, *J. Mater. Chem. A*, 2018, **6**, 1816–1821.

31 Z. Q. Shi, N. N. Ji, M. H. Wang and G. Li, A comparative study of proton conduction between a 2D Zinc(II) MOF and its corresponding organic ligand, *Inorg. Chem.*, 2020, **59**, 4781–4789.

32 X. Wang, T. Qin, S. S. Bao, Y. C. Zhang, X. Shen, L. M. Zheng and D. Zhu, Facile synthesis of a water stable 3D Eu-MOF showing high proton conductivity and its application as a sensitive luminescent sensor for Cu^{2+} ions, *J. Mater. Chem. A*, 2016, **4**, 16484–16489.

33 A. Shigematsu, T. Yamada and H. Kitagawa, Wide control of pro-ton conductivity in porous coordination polymers, *J. Am. Chem. Soc.*, 2011, **133**, 2034–2036.

34 P. V. Rijn, M. Tutus, C. Kathrein, L. Zhu, M. Wessling, U. Schwaneberg and A. Böker, Challenges and advances in the field of self-assembled membranes, *Chem. Soc. Rev.*, 2013, **42**, 6578–6592.

35 D. W. Lim, M. Sadakiyo and H. Kitagawa, Proton transfer in hydro-gen-bonded degenerate systems of water and ammonia in metal-organic frameworks, *Chem. Sci.*, 2019, **10**, 16–33.

36 S. P. Bera, A. Mondal, S. Roy, B. Dey, A. Santra and S. Konar, 3D isomorphous lanthanide coordination polymers displaying magnetic refrigeration, slow magnetic relaxation and tunable proton conduction, *Dalton Trans.*, 2018, **47**, 15405–15415.

37 Y. Ye, X. Wu, Z. Yao, L. Wu, Z. Cai, L. Wang, X. Ma, Q. H. Chen, Z. Zhang and S. Xiang, Metal-organic frameworks with a large breathing effect to host hydroxyl compounds for high anhydrous proton conductivity over a wide temperature range from subzero to 125 °C, *J. Mater. Chem. A*, 2016, **4**, 4062–4070.

38 D. Umeyama, S. Horike, M. Inukai, Y. Hijikata and S. Kitagawa, Confinement of mobile histamine in coordination nanochannels for fast proton transfer, *Angew. Chem., Int. Ed.*, 2011, **50**, 11706–11709.

39 H. B. Luo, Q. Ren, P. Wang, J. Zhang, L. Wang and X. M. Ren, High proton conductivity achieved by encapsulation of imidazole molecules into proton-conducting MOF-808, *ACS Appl. Mater. Interfaces*, 2019, **11**, 9164–9171.

40 Z. Zhang, J. Ren, J. Xu, Z. Wang, W. He, S. Wang, X. Yang, X. Du, L. Meng and P. Zhao, Adjust the arrangement of imidazole on the metal-organic framework to obtain hybrid proton exchange membrane with long-term stable high proton conductivity, *J. Membr. Sci.*, 2020, **607**, 118194–118207.

41 S. Chandra, T. Kundu, S. Kandambeth, R. BabaRao, Y. Marathe, S. M. Kunjir and R. Banerjee, Phosphoric acid loaded azo (−N=N−) based covalent organic framework for proton conduction, *J. Am. Chem. Soc.*, 2014, **136**, 6570–6573.

42 H. Ma, B. Liu, B. Li, L. Zhang, Y. G. Li, H. Q. Tan, H. Y. Zang and G. Zhu, Cationic covalent organic frameworks: a simple platform of anionic exchange for porosity tuning and proton conduction, *J. Am. Chem. Soc.*, 2016, **138**, 5897–5903.

43 A. L. Li, Q. Gao, J. Xu and X. H. Bu, Proton-conductive metal-organic frameworks: recent advances and perspectives, *Coord. Chem. Rev.*, 2017, **344**, 54–82.

44 F. F. Zhang, Z. K. Tu, J. Yu, H. B. Li, C. Huang and H. N. Zhang, Impregnation of imidazole functionalized polyhedral oligomeric silsesquioxane in polymer electrolyte membrane for elevated temperature fuel cells, *RSC Adv.*, 2013, **3**, 5438–5446.

45 F. Yang, H. Huang, X. Wang, F. Li, Y. Gong, C. Zhong and J. Li, Proton conductivities in functionalized UiO-66: tuned properties, thermogravimetry mass, and molecular simulation analyses, *Cryst. Growth Des.*, 2015, **15**, 5827–5833.

46 F. Yang, G. Xu, Y. Dou, B. Wang, H. Zhang, H. Wu, W. Zhou, J. Li and B. Chen, A flexible metal-organic framework with a high densi-ty of sulfonic acid sites for proton conduction, *Nat. Energy*, 2017, **2**, 877–883.

47 X. Y. Dong, X. P. Hu, H. C. Yao, S. Q. Zang, H. W. Hou and T. C. W. Mak, Alkaline earth metal (Mg, Sr, Ba)-organic frameworks based on 2,2′,6,6′-tetracarboxybiphenyl for proton conduction, *Inorg. Chem.*, 2014, **53**, 12050–12057.

48 F. M. Zhang, L. Z. Dong, J. S. Qin, W. Guan, J. Liu, S. L. Li, M. Lu, Y. Q. Lan, Z. M. Su and H. C. Zhou, Effect of imidazole arrange-ments on proton-conductivity in metal-organic frameworks, *J. Am. Chem. Soc.*, 2017, **139**, 6183–6189.

49 Z. G. Shao, P. Joghee and I. M. Hsing, Preparation and characterization of hybrid Nafion-silica membrane doped with phosphotungstic acid for high temperature operation of proton exchange membrane fuel cells, *J. Membr. Sci.*, 2004, **229**, 43–51.

50 P. Ramaswamy, N. E. Wong, B. S. Gelfand and G. K. H. Shimizu, A water stable magnesium MOF that conducts protons over 10^{-2} S cm^{-1}, *J. Am. Chem. Soc.*, 2015, **137**, 7640–7643.

51 S. Liu, Z. Yuea and Y. Liu, Incorporation of imidazole within the metal-organic framework UiO-67 for enhanced anhydrous proton conductivity, *Dalton Trans.*, 2015, **44**, 12976–12980.